

A Kinetic Method for Hyperbolic–Elliptic Equations and Its Application in Two-Phase Flow

K. Xu

*Mathematics Department, Hong Kong University of Science and Technology,
Clear Water Bay, Kowloon, Hong Kong, China
E-mail: makxu@uxmail.ust.hk*

Received August 12, 1999; revised October 12, 2000

A kinetic method for hyperbolic–elliptic equations is presented in this paper. In the mixed type system, the coexistence of liquid and gas and the phase transition between them are described by the van der Waals-type equation of state (EOS). Because the fluid is unstable in the elliptic region, the interface between liquid and gas can be captured naturally through condensation and evaporation processes, which continuously remove any “averaged” numerical fluid away from the elliptic region at the interfaces. As a result, a sharp liquid–gas interface can be constructed from the competition between the numerical diffusion and phase transition. The numerical examples presented in this paper include both phase transition and multifluid interface problems. © 2001 Academic Press

Key Words: van der Waals equation of state; phase transition; interface capturing; kinetic scheme.

1. INTRODUCTION

The study of liquid–gas phase transition and interface movement is important in science and engineering. The macroscopic governing equations studied in the current paper are the mixed hyperbolic–elliptic system, where the van der Waals-type equation of state is used. Many numerical schemes have been proposed to solve the mixed type system, and the search for the possible Riemann solution for such a system is still under investigation [9, 10, 12, 16, 18, 27, 29, 30]. To properly capture the density jump across a liquid–gas interface, as well as satisfy the equal-area rule in the Maxwell construction, the viscosity and capillarity condition has been proposed, especially for 1D flow [28]. To capture the physical realizable solution, many problems, such as the entropy rate admissibility condition and the interface stability problem, have been well analyzed theoretically; see [3] and references therein.

Physically, dense gas properties, such as phase transition behavior and surface tension, can be derived from the microscopic Boltzmann equation [6]. For example, the van der Waals model can be rigorously obtained from statistical mechanics, and the coexistence region of liquid and gas is predicted from the Maxwell construction. Particle interaction with nearby repulsion and long-ranged attraction can naturally represent the phase transition and surface tension properties [11, 20]. However, because of the extreme complexity of the collision kernel of the interacting particles in a dense gas and the tremendous computer resources required to resolve the six-dimensional distribution function, many kinetic methods are mainly used for computations with an ideal compressible gas [34]. Recently, He *et al.* have simplified the Boltzmann equation for a dense gas and implemented the intermolecular interaction as a source term into the gas–kinetic BGK model [13], from which both the van der Waals equation of state (EOS) and the surface tension can be obtained. Based on the simple particle interaction pictures, many lattice Boltzmann methods (LBM) have been developed (see [7, 21, 25, 26, 32] and references therein) and the particle interaction mechanism is used to simulate the phase transition and multiphase flow. Recently, combining the macroscopic van der Waals equation of state and the mesoscopic lattice Boltzmann method, He *et al.* developed an interesting scheme for capturing the liquid–gas interface and have successfully applied the scheme to the study of the Rayleigh–Taylor instability [14]. Similar to the volume of fluid (VOF) and level set methods [15, 24], an index function is used in [14] to capture the liquid–gas interface, but the possible phase transition has not been studied there. Also, the densities of the liquid and gas in [14] are assigned numerically with values which may not be consistent with the ones from the van der Waals EOS and the Maxwell construction. In the past decades, many interface capturing and sharpening schemes have been developed. The level set method is one of the most successful ones in the multifluid applications (see [17, 19, 31] and references therein). The reinitialization procedure used in the level set method could keep the level set as a distance function and significantly reduce the mass losses caused by using the material velocity for advection of the level set function instead of the interfacial velocity.

In this paper, we develop a kinetic BGK-type scheme [34] for the hyperbolic–elliptic system, where the continuum and momentum equations are solved by following the time evolution of the gas distribution function of the approximate Boltzmann equation. The phase transition and motion of the multifluid interface are captured naturally in the current method. However, as the result of the van der Waals EOS considered here, the current method can only be applied to the equilibrium phase transition problem. It is inadequate for understanding the nonequilibrium process inside the liquid–gas interface. Also, the BGK model used in the current study is only one of the kinetic models that can be employed to study multiphase flow. The kinetic equation derived in [13] has more generality, which can be used as a starting point.

2. GOVERNING EQUATIONS AND INTERFACE CAPTURING MECHANISM

In the one-dimensional case, the governing equations for the isothermal hyperbolic–elliptic system are

$$\begin{pmatrix} \rho \\ \rho U \end{pmatrix}_t + \begin{pmatrix} \rho U \\ \rho U^2 + p \end{pmatrix}_x = 0, \quad (1)$$

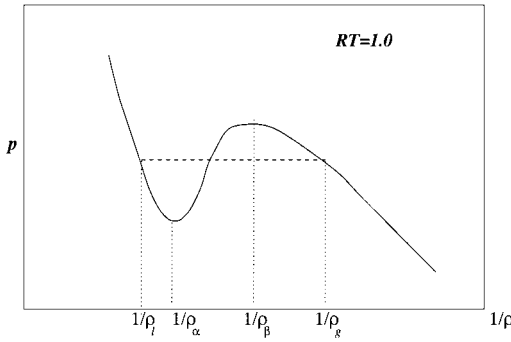


FIG. 1. The van der Waals equation of state for $RT = 1.0$ case.

where ρ and U are the density and velocity. For multiphase flow and phase transition problems, the relation between the pressure p and the density proposed by van der Waals is quite satisfactory. The equation of state is

$$p = \frac{\rho RT}{1 - b\rho} - a\rho^2,$$

where R is the gas constant, T is the temperature, and a and b are constants. The critical temperature for the separation of liquid and gas is

$$T_c = \frac{8a}{27bR}.$$

When the fluid temperature is below the critical value, phase segregation occurs. In this paper, we study fluids with fixed values $a = 0.9$, $b = 0.25$, and $RT = 1.0$. The corresponding critical temperature in this case is $T_c = 1.0666/R$. Since RT is less than $T_c R$, the phase transition can appear in the current fluid system. An illustrative plot of the van der Waals EOS is shown in Fig. 1. The densities of liquid ρ_l and gas ρ_g can be obtained from the Maxwell construction (equal-area construction). The values in the plot are $1/\rho_l = 0.494273$, $1/\rho_g = 1.405065$, $1/\rho_\alpha = 0.574912$, and $1/\rho_\beta = 1.036251$. The fluid density ρ can be catalogued in the following regions:

$$\begin{aligned}
 \frac{1}{\rho} < \frac{1}{\rho_l}, & \quad \text{liquid phase,} \\
 \frac{1}{\rho_l} < \frac{1}{\rho} < \frac{1}{\rho_\alpha}, & \quad \text{metastable region,} \\
 \frac{1}{\rho_\alpha} < \frac{1}{\rho} < \frac{1}{\rho_\beta}, & \quad \text{unstable elliptic region (mixture),} \\
 \frac{1}{\rho_\beta} < \frac{1}{\rho} < \frac{1}{\rho_g}, & \quad \text{metastable region,} \\
 \frac{1}{\rho_g} < \frac{1}{\rho}, & \quad \text{gas phase.}
 \end{aligned} \tag{2}$$

When the fluid density takes on values in the elliptical region, any small fluid perturbation will be amplified owing to the negative slope of $\partial p/\partial \rho$. The fluid mixture in the elliptic region will either evaporate to the gas or condense to the liquid. So, similar to the shock-steepening mechanism, the van der Waals EOS has an intrinsic physical mechanism to

separate different phases at the multifluid interface and sharpen the interface. This is the physical reason for the existence of the sharp liquid–gas interface in the real world. This property can also be used to develop an interface capturing scheme.

Numerically, because of cell size limitations and the averaging process [34], the liquid and gas inside any numerical cell are mixed to form an averaged state. If there is no steepening mechanism to separate the mixed fluid, such as at the contact discontinuity wave of the compressible Euler equations, the thickness of the interface will grow with the square root of evolution time or total number of numerical time steps. Physically, the liquid–gas interface is kept sharp through molecular interaction in the microscopic description or through the van der Waals-type EOS in the macroscopic equations. Once this kind of physics is incorporated into a numerical scheme for the multifluid motion, the averaged state which most likely happens in the elliptical region will condense to the liquid or evaporate to the gas, and a sharp interface can be obtained automatically.

To use this kind of steepening mechanism, any proposed scheme must be accurate in predicting the liquid and gas densities first. In other words, even without explicit terms for the Maxwell equal-area construction in Eq. (1), any scheme must have certain intrinsic dissipative or diffusion mechanisms to pick up the physical solution with the correct density jump. Mathematically, the correct density jump at the interface can be obtained through the implementation of the viscosity capillarity condition. For example, in the 1D case and in the Lagrangian formulation [28], the momentum equation should have terms $\epsilon U_{xx} - \epsilon^2 A(1/\rho)_{xxx}$ on the right-hand side, where ϵ denotes viscosity and $\epsilon^2 A$ is the capillarity coefficient. In the multidimensional case, the capillarity term is similar to the term related to the surface tension. However, even in the case without surface tension, such as the 1D case, the above viscosity capillarity condition is still necessary for the correct density jump at a interface. It has been shown theoretically that the above viscosity capillarity condition is equivalent to the inclusion of diffusion and dissipative terms in the mass and momentum equations, where the dissipative coefficients have to satisfy certain conditions [29].

Currently, it seems difficult for any high-order scheme to predict a very accurate density jump at a multifluid interface. It is not surprising that many existing high-order schemes will have numerical viscosity and diffusion coefficients which strongly depend on the interpolation limiters, CFL number, cell size, and even the Runge–Kutta time-stepping techniques. In the current paper, we present a kinetic scheme to solve Eq. (1). Because of the special diffusion and dissipative mechanisms in the kinetic approach, the Maxwell equal-area rule seems to be implicitly achieved. The resulting equilibrium densities of liquid and gas are very close to the theoretical values. At the same time, the phase boundary can be kept within two or three grid points. After verification of this property, the kinetic method is used to simulate the evolution of a multifluid interface. The interface captured in the current method is a numerical interface. The exact magnitude of the numerical diffusion and its effect on the physical capillarity is difficult to estimate. Anderson, McFadden, and Wheeler presented an excellent introduction and review for more realistic diffuse interface models derived from the thermodynamics [1].

3. KINETIC SCHEME FOR THE HYPERBOLIC–ELLIPTIC EQUATIONS

The kinetic BGK model of the approximate Boltzmann equation is [2]

$$f_t + u f_x = \frac{g - f}{\tau}, \quad (3)$$

where f is the gas distribution function, g is the equilibrium state, and τ is the particle collision time. Both f and g are functions of space x , time t , and particle velocity u . The macroscopic variables, such as ρ , U , and p in Eq. (1), are the moments of the above gas distribution function defined by the relations

$$\rho = \int f \, du, \quad U = \frac{\int u f \, du}{\rho}, \quad p = \int (u - U)^2 f \, du.$$

To recover Eq. (1) from Eq. (3), we can construct an equilibrium state

$$g = \rho \left(\frac{\lambda}{\pi} \right)^{\frac{1}{2}} e^{-\lambda(u-U)^2},$$

where λ is defined by

$$\begin{aligned} \lambda &= \frac{\rho}{2p} \\ &= \frac{1}{2} \frac{1 - b\rho}{RT - a\rho + ab\rho^2} \\ &= \Lambda(\rho), \end{aligned} \tag{4}$$

and the variation of λ is related to the density changes by

$$\begin{aligned} d\lambda &= \frac{1}{2} \frac{ab^2\rho^2 - 2ab\rho + (a - bRT)}{(RT - a\rho + ab\rho^2)^2} d\rho \\ &= D(\rho)d\rho, \end{aligned} \tag{5}$$

where the functions Λ and D are well defined in the above equations. In the current paper, a fixed value $RT = 1.0$ is used.

Because both mass and momentum must be conserved during the particle collision, f and g satisfy the compatibility condition

$$\int (f - g)\psi \, du = 0 \quad \text{for } \psi = (1, u)^T, \tag{6}$$

at any point in space and time.

The solution of the BGK model (3) is

$$f(x_{j+1/2}, t, u) = \frac{1}{\tau} \int_0^t g(x', t', u) e^{-(t-t')/\tau} dt' + e^{-t/\tau} f_0(x_{j+1/2} - ut), \tag{7}$$

where $x_{j+1/2}$ is the location of the cell interface and $x' = x_{j+1/2} - u(t - t')$ is the particle trajectory. There are two unknowns in the above equation. One is the initial gas distribution function f_0 at time $t = 0$, and the other is g in both space and time locally around $(x_{j+1/2}, t = 0)$. Similar to the BGK-type schemes for the Euler and Navier–Stokes equations [34], the numerical scheme based on Eq. (7), along with the compatibility condition (6), is described as follows:

Step 1: Use the MUSCL technique [33] to interpolate the conservative variables $W = (\rho, \rho U)^T$, and obtain the reconstructed initial data inside each cell,

$$W_j(x) = W_j(x_j) + \frac{W_j(x_{j+1/2}) - W_j(x_{j-1/2})}{x_{j+1/2} - x_{j-1/2}}(x - x_j) \quad \text{for } x \in [x_{j-1/2}, x_{j+1/2}], \tag{8}$$

where $W_j(x_j)$ is the cell-averaged value, and $W_j(x_{j-1/2})$ and $W_j(x_{j+1/2})$ are the values at the left and right boundaries of cell j , which are constructed using a nonlinear limiter, such as van Leer's limiter. After the reconstruction, the values ρ , U and their corresponding slopes, e.g., $\partial\rho/\partial x$ and $\partial U/\partial x$, are obtained. Therefore, the variation λ can be found subsequently through Eq. (5), as $\partial\lambda/\partial x = D(\rho)\partial\rho/\partial x$.

Step 2: Based on the reconstructed data in Step 1, around each cell interface $x_{j+1/2}$, the initial gas distribution function f_0 is assumed to be

$$f_0(x) = \begin{cases} g^l [1 + (x - x_{j+1/2})a^l], & x \leq x_{j+1/2}, \\ g^r [1 + (x - x_{j+1/2})a^r], & x \geq x_{j+1/2}, \end{cases} \quad (9)$$

where the states g^l and g^r are the Maxwellian distribution functions defined in terms of the conservative variables at a cell interface,

$$g^l = g^l(W_j(x_{j+1/2})) \quad \text{and} \quad g^r = g^r(W_{j+1}(x_{j+1/2})). \quad (10)$$

For example, with the distribution

$$g^l = \rho^l \left(\frac{\lambda^l}{\pi} \right)^{\frac{1}{2}} e^{-\lambda^l(u-U^l)^2}, \quad (11)$$

all coefficients in g^l can be obtained as

$$\begin{pmatrix} \rho^l \\ U^l \\ \lambda^l \end{pmatrix} = \begin{pmatrix} \rho_j(x_{j+1/2}) \\ \rho_j U_j(x_{j+1/2}) / \rho_j(x_{j+1/2}) \\ \Lambda(\rho^l) \end{pmatrix}. \quad (12)$$

Similar formulation can be found for g^r . The coefficients $a^{l,r}$ in Eq. (9) have the forms

$$a^{l,r} = m_1^{l,r} + m_2^{l,r}u + m_3^{l,r}u^2, \quad (13)$$

which can be obtained from the Taylor expansion of a Maxwellian distribution function. The coefficients $(m_1^{l,r}, m_2^{l,r}, m_3^{l,r})$ depend on (ρ^l, U^l) , (ρ^r, U^r) and their corresponding slopes, i.e.,

$$\left(\frac{\partial\rho^l}{\partial x}, \frac{\partial U^l}{\partial x}, \frac{\partial\lambda^l}{\partial x} \right) \quad \text{and} \quad \left(\frac{\partial\rho^r}{\partial x}, \frac{\partial U^r}{\partial x}, \frac{\partial\lambda^r}{\partial x} \right).$$

The detailed relations are

$$\begin{aligned} m_1^{l,r} &= \left[\frac{1}{\rho} \left(\frac{\partial\rho}{\partial x} \right) + \left(\frac{1}{2\lambda} - U^2 \right) \frac{\partial\lambda}{\partial x} - 2\lambda U \frac{\partial U}{\partial x} \right]^{l,r}, \\ m_2^{l,r} &= \left[2U \frac{\partial\lambda}{\partial x} + 2\lambda \frac{\partial U}{\partial x} \right]^{l,r}, \\ m_3^{l,r} &= \left[-\frac{\partial\lambda}{\partial x} \right]^{l,r}. \end{aligned} \quad (14)$$

Therefore, with the initially reconstructed data in Step 1, $f_0(x)$ in Eq. (9) is totally determined. For the sake of simplicity, we assume $x_{j+1/2} = 0$ in the rest of this paper.

Step 3: The equilibrium state g is constructed as

$$g = g_0[1 + (1 - \mathbf{H}[x])\bar{a}^l x + \mathbf{H}[x]\bar{a}^r x + \bar{A}t], \quad (15)$$

where $\mathbf{H}[x]$ is the Heaviside function and g_0 is the state located at $(x = 0, t = 0)$:

$$g_0 = \rho_0 \left(\frac{\lambda_0}{\pi} \right)^{\frac{1}{2}} e^{-\lambda_0(u-U_0)^2}. \quad (16)$$

The coefficients \bar{a}^l , \bar{a}^r , and \bar{A} in Eq. (15) have the forms

$$\begin{aligned} \bar{a}^{l,r} &= \bar{m}_1^{l,r} + \bar{m}_2^{l,r} u + \bar{m}_3^{l,r} u^2, \\ \bar{A} &= \bar{A}_1 + \bar{A}_2 u + \bar{A}_3 u^2, \end{aligned}$$

which have the same functional dependence on $(\partial\rho/\partial x, \partial U/\partial x)$ and $(\partial\rho/\partial t, \partial U/\partial t)$ as shown in Eqs. (13) and (14).

Taking both limits $(x \rightarrow 0)$ and $(t \rightarrow 0)$ in Eqs. (7) and (15), and applying the compatibility condition at $(x = 0, t = 0)$, we can get macroscopic quantities

$$W_0 = \begin{pmatrix} \rho_0 \\ \rho_0 U_0 \end{pmatrix} = \int g_0 \psi \, du = \int (g^l \mathbf{H}[u] + g^r (1 - \mathbf{H}[u])) \psi \, du, \quad (17)$$

where g^l and g^r are known from Step 2. Here W_0 is the ‘‘averaged’’ flow variables at the cell interface, from which g_0 can be determined. Then, connecting W_0 to the cell-centered values $W_j(x_j)$ and $W_{j+1}(x_{j+1})$, we can get the slopes for mass and momentum distributions on both sides,

$$\begin{aligned} \left(\frac{\partial \rho_0^l}{\partial x}, \frac{\partial (\rho_0 U_0)^l}{\partial x} \right)^T &= \frac{W_0 - W_j(x_j)}{x_{j+1/2} - x_j} \quad \text{for } x \leq 0, \\ \left(\frac{\partial \rho_0^r}{\partial x}, \frac{\partial (\rho_0 U_0)^r}{\partial x} \right)^T &= \frac{W_{j+1}(x_{j+1}) - W_0}{x_{j+1} - x_{j+1/2}} \quad \text{for } x \geq 0, \end{aligned} \quad (18)$$

from which $\partial\rho/\partial x$, $\partial U/\partial x$, and $\partial\lambda/\partial x$ can be obtained. Therefore, (\bar{a}^l, \bar{a}^r) in Eq. (15) can be determined in a similar way to that in Eqs. (13) and (14). The only unknown in Eq. (15) is \bar{A} , which is related to $\partial\rho_0/\partial t$, $\partial U_0/\partial t$, and $\partial\lambda_0/\partial t$ ($=D(\rho_0)\partial\rho_0/\partial t$) through the relations

$$\begin{aligned} \bar{A}_1 &= \left[\frac{1}{\rho_0} \left(\frac{\partial \rho_0}{\partial t} \right) + \left(\frac{1}{2\lambda_0} - U_0^2 \right) \frac{\partial \lambda_0}{\partial t} - 2\lambda_0 U_0 \frac{\partial U_0}{\partial t} \right]^{l,r}, \\ \bar{A}_2 &= \left[2U_0 \frac{\partial \lambda_0}{\partial t} + 2\lambda_0 \frac{\partial U_0}{\partial t} \right]^{l,r}, \\ \bar{A}_3 &= \left[-\frac{\partial \lambda_0}{\partial t} \right]^{l,r}. \end{aligned} \quad (19)$$

To this point, we need to evaluate $\partial\rho_0/\partial t$ and $\partial(\rho U)_0/\partial t$.

Step 4: Substituting Eqs. (15) and (9) into the integral solution (7), we obtain the distribution function f at $x = 0$,

$$\begin{aligned} f(0, t, u) &= \gamma_0 g_0 + \gamma_1 (\bar{a}^l \mathbf{H}[u] + \bar{a}^r (1 - \mathbf{H}[u])) u g_0 + \gamma_2 \bar{A} g_0 + \gamma_3 ((1 - ut a^l) \mathbf{H}[u] g^l \\ &\quad + (1 - ut a^r) (1 - \mathbf{H}[u]) g^r), \end{aligned} \quad (20)$$

where

$$\begin{aligned}\gamma_0 &= 1 - e^{-t/\tau}, \\ \gamma_1 &= \tau(-1 + e^{-t/\tau}) + te^{-t/\tau}, \\ \gamma_2 &= \tau(t/\tau - 1 + e^{-t/\tau}), \\ \gamma_3 &= e^{-t/\tau}.\end{aligned}$$

The only unknown in Eq. (20) is \bar{A} , which is a function of $(\partial\rho_0/\partial t, \partial U_0/\partial t)$ (see Eq. (19)). Since the compatibility condition must be satisfied everywhere in space and time, it can be integrated in a whole CFL time step ΔT at $x = 0$:

$$\int_0^{\Delta T} \int (f(0, t, u) - g(0, t, u))\psi dt du = 0. \quad (21)$$

From this we obtain

$$\begin{aligned}\left(\Gamma_5 \frac{\partial\rho_0}{\partial t}, \Gamma_5 \frac{\partial(\rho U)_0}{\partial t}\right)^T &= \int [-\Gamma_3 g_0 + \Gamma_1 u(\bar{a}^1 H[u] + \bar{a}^r(1 - H[u]))g_0 \\ &\quad + \Gamma_3(H[u]g^l + (1 - H[u])g^r) + \Gamma_4 u(a^1 H[u]g^l \\ &\quad + a^r(1 - H[u])g^r)]\psi du.\end{aligned} \quad (22)$$

All terms on the right-hand side of the above equation are known, and

$$\begin{aligned}\Gamma_0 &= \Delta T - \tau(1 - e^{-\Delta T/\tau}), \\ \Gamma_1 &= \tau(-\Delta T + 2\tau(1 - e^{-\Delta T/\tau}) - \Delta T e^{-\Delta T/\tau}), \\ \Gamma_2 &= \frac{1}{2}\Delta T^2 - \tau\Delta T + \tau^2(1 - e^{-\Delta T/\tau}), \\ \Gamma_3 &= \tau(1 - e^{-\Delta T/\tau}), \\ \Gamma_4 &= -\tau(-\Delta T e^{-\Delta T/\tau} + \tau(1 - e^{-\Delta T/\tau})), \\ \Gamma_5 &= \tau(\Delta T - \tau(1 - e^{-\Delta T/\tau})).\end{aligned}$$

Thus, $(\partial\rho_0/\partial t, \partial U_0/\partial t)$, as well as $\partial\lambda_0/\partial t$, can be obtained from Eq. (22).

Step 5: The time-dependent numerical fluxes of mass and momentum across the cell interface are

$$F_{W,j+1/2} = \begin{pmatrix} F_\rho(t) \\ F_{\rho U}(t) \end{pmatrix}_{j+1/2} = \int u\psi f_{j+1/2}(0, t, u) du, \quad (23)$$

where f is given in Eq. (20). The update of flow variables inside each cell becomes

$$W_j^{n+1} = W_j^n + \frac{1}{\Delta x} \int_0^{\Delta t} (F_{W,j-1/2} - F_{W,j+1/2}) dt.$$

From the above updated variables W_j^{n+1} , Steps 1–5 can be repeated again at the next time level.

4. NUMERICAL EXAMPLES

In this section, we present a few test cases in both one and two dimensions. The van Leer limiter is used for the interpolations of ρ and ρU at the beginning of each time step. The time step ΔT is determined by the Courant–Friedrichs–Levy condition with CFL number 0.5 for the 1D cases and 0.25 for the 2D cases. The collision time τ is defined by

$$\tau = C_1 \Delta T + C_2 \Delta T \frac{|p^l - p^r|}{p^l + p^r}, \tag{24}$$

where $p^l = \Lambda(\rho^l)$, $p^r = \Lambda(\rho^r)$, and $C_1 = 0.05$ and $C_2 = 2.0$ are fixed in all calculations.

4.1. 1D Shock Tube Cases

In the following, we apply the kinetic method to four shock tube cases, which are used by Shu [27] for testing the ENO-type schemes. In all four cases, the computational domain is $x \in [0, 1]$. There are 200 grid points used in the first three cases and the corresponding cell size is $\Delta x = 1/200$. For the fourth case, 400 grid points are used and the cell size is $\Delta x = 1/400$.

Case 1. The initial condition for this case is the exact liquid and gas densities from the Maxwell construction, where the initial data are given by

$$(1/\rho_L = 0.494273, U_L = 1.0)|_{x < 0.125} \quad \text{and} \quad (1/\rho_R = 1.405065, U_R = 1.0)|_{x > 0.125}.$$

This test is mainly used to see if the scheme can keep the admissible density jump from the Maxwell construction. At the output time $t = 0.60$, the density distribution (connected circles) is shown in Fig. 2, where the dashed and dotted lines represent $1/\rho_1$, $1/\rho_g$, $1/\rho_\alpha$, and $1/\rho_\beta$ respectively.

Case 2. The second case has the following initial condition:

$$(1/\rho_L = 0.54, U_L = 1.0)|_{x < 0.125} \quad \text{and} \quad (1/\rho_R = 1.8517, U_R = 1.0)|_{x > 0.125}.$$

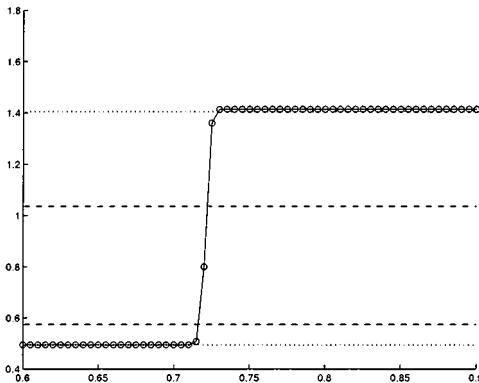


FIG. 2. Connected circles are the calculated distribution of $1/\rho$ with a cell size $\Delta x = 1/200$ at the output time $t = 0.60$. The initial density discontinuity is located at $x = 0.125$. The dotted lines are densities of $1/\rho_1$ and $1/\rho_g$ from the Maxwell construction. The region between the dashed lines ($1/\rho_\alpha$, $1/\rho_\beta$) is the elliptic region where the fluid is intrinsically unstable.

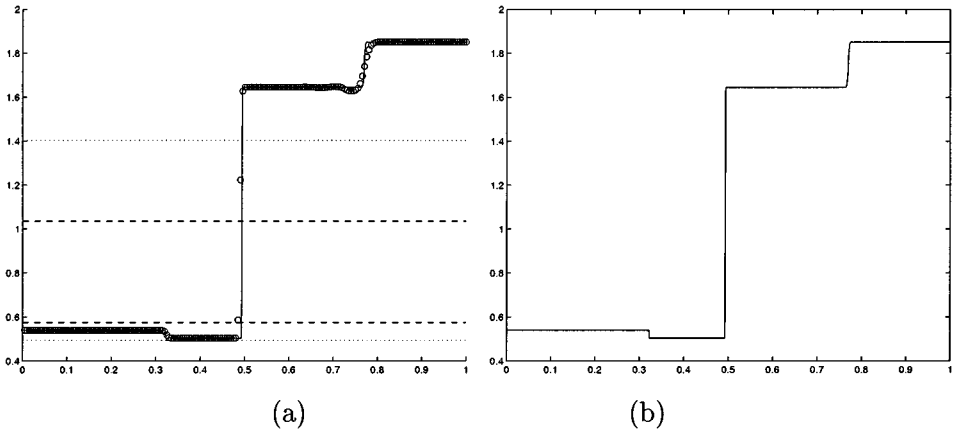


FIG. 3. (a) Circles are the simulation results of distribution $1/\rho$, which are obtained from a calculation with the cell size $\Delta x = 1/200$ at the output time $t = 0.50$. The solid line is the result obtained with a much refined mesh $\Delta x = 1/2000$. (b) Distribution of $1/\rho$ obtained with a refined mesh $\Delta x = 1/2000$. The solid lines in (a) and (b) are the same line.

This initial jump satisfies the Rankine–Hugoniot condition but does not satisfy the density jump from the Maxwell construction (viscosity capillarity condition). The simulation results at time $t = 0.5$ are shown in Fig. 3a, where the solid line is obtained with the same scheme but on a much refined mesh $\Delta x = 1/2000$. In Fig. 3b, the density calculated with the refined mesh $\Delta x = 1/2000$ is shown separately to aid comparison with the results in [27]. This case clearly shows that the current scheme can pick up the physically admissible solution. There are no oscillations at the liquid–gas interface.

Case 3. The initial condition for this case is

$$(1/\rho_L = 0.45, U_L = 1.0)|_{x < 0.125} \quad \text{and} \quad (1/\rho_R = 2.0, U_R = 2.0)|_{x > 0.125}.$$

Figure 4 shows the density distribution at the output time $t = 0.30$, and the solid line is the solution obtained from a calculation with a refined mesh $\Delta x = 1/2000$. From this figure, we can also observe the sharp interface between the liquid and gas phases.

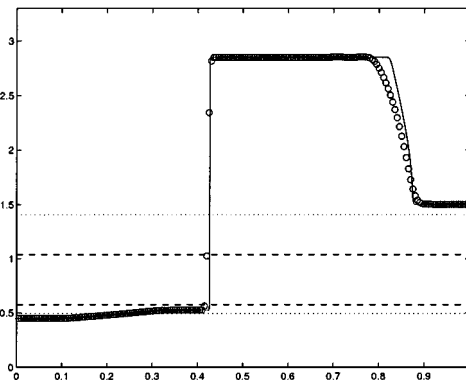


FIG. 4. Circles are distribution of $1/\rho$ calculated with a cell size $\Delta x = 1/200$ at the output time $t = 0.30$. The solid line is the result obtained with a refined mesh $\Delta x = 1/2000$.

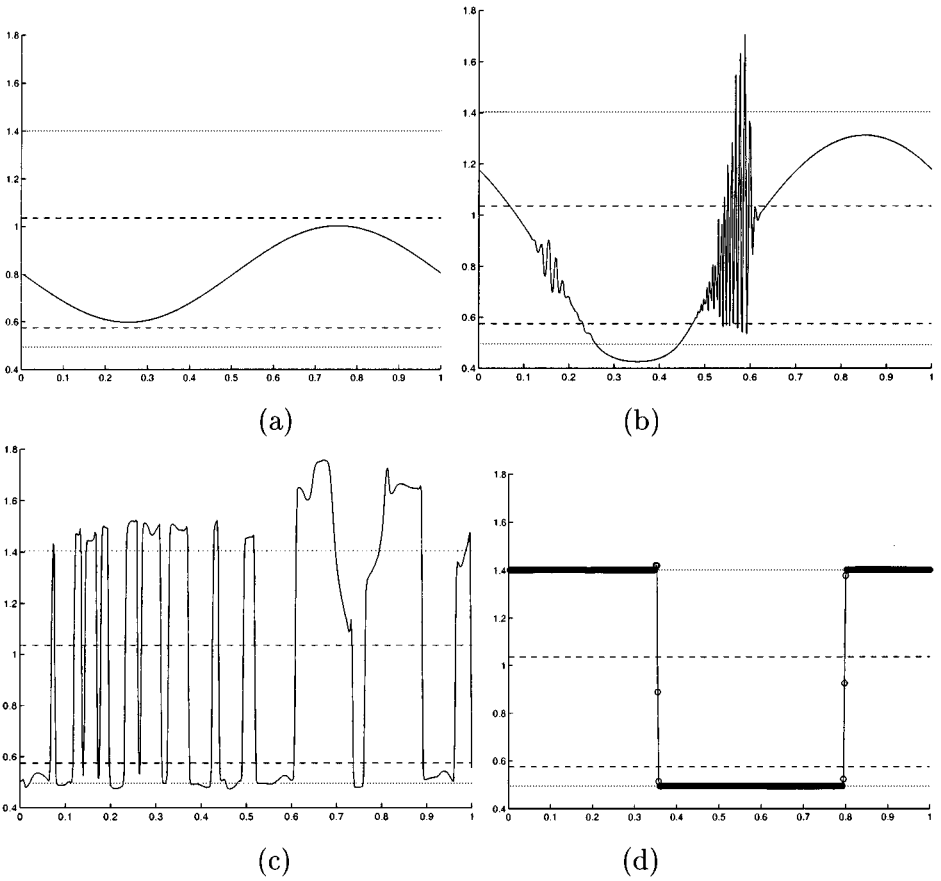


FIG. 5. The solid lines are the distributions of $1/\rho$ at different output times. The mesh size used is $\Delta x = 1/400$. (a) $t = 0.0$; (b) $t = 0.1$; (c) $t = 1.0$; (d) $t = 100.0$. Circles are added in plot (d) to show the number of grid points around the liquid–gas interfaces.

Case 4. The initial condition for this case is

$$(1/\rho, U) = (0.8 + 0.2 \sin(x), 1 - 0.5 \cos(x)).$$

The initial density is entirely in the elliptic region. Periodic boundary conditions are used. The solutions with cell size $\Delta x = 1/400$ at different output time are shown in Fig. 5. These figures clearly show the flow instability in the elliptic region and how the densities eventually go to the well-defined liquid and gas densities, even though the Maxwell construction is not explicitly used in the current scheme. For the liquid and gas phases, the numerical densities obtained at time $t = 100$ are $1/\rho = (0.49400, 1.40175)$. The differences between the numerical values and the theoretical ones $(0.494273, 1.405065)$ are less than 0.5%. This is a very good case to test the ability of any high-order scheme to capture the correct density jumps around the phase boundary, as well as the sharpness of the interface. Our scheme can capture the jump within 2 or 3 cells, as shown in Fig. 5d.

4.2. Liquid–Gas Interfaces in 2D Cases

In 2D cases, the inclusion of surface tension and gravity becomes important. In test case 5, the gravitational force ρG is implemented in the y -momentum equation for the

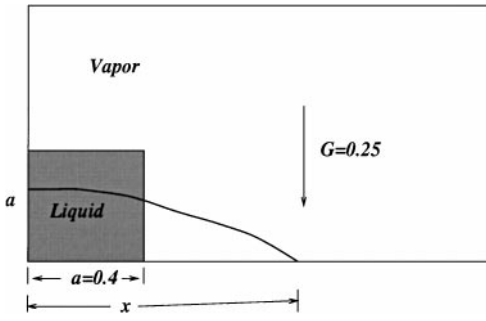


FIG. 6. Schematic diagram of liquid–gas distributions.

liquid phase, and the nondimensional magnitude of G is assigned the value 0.25. In test case 6, an additional body force $\kappa\rho\nabla\nabla^2\rho$ is added in the momentum equations to recover the surface tension effect [7, 14, 23]. The nondimensional coefficient κ used in case 6 is equal to 5.0×10^{-6} .

Case 5. This is a dam break problem. Many schemes have been used in this kind of free surface problem, including the volume of fluid (VOF) method, boundary integral techniques, the front tracking method, and the arbitrary Lagrangian–Eulerian (ALE) method (see [4, 8, 15, 35] and references therein). The cell size used in our study is $\Delta x = \Delta y = 1/100$. The schematic construction for this problem is shown in Fig. 6, where the densities of the liquid and gas are assigned the values from the Maxwell construction, i.e., $1/\rho_l = 0.494273$ and $1/\rho_g = 1.405065$. The initial velocity of both gas and liquid are zero, and no surface tension is included in this case. Owing to numerical diffusion, any index function used to describe the liquid and gas interface will get smeared in the Eulerian advection scheme, and the smearing is proportional to the square root of the number of time steps used. To overcome this difficulty, the level set method employs an intelligent interface sharpening mechanism [5]. In our case, since the van der Waals EOS is used to describe the liquid and gas phases, any smeared density at the interface is most likely to occur in the elliptic region and the flow instability in these region will automatically steepen the interface. More specifically, the condensation and evaporation processes around the phase boundary could move the averaged density to the liquid or gas phases, and this effect compensates the numerical dissipation in the advection scheme. Figure 7 shows the time evolution of the liquid–gas interface, and the interface thickness is two or three mesh points regardless of the time steps used to get the final results. Figure 8 shows the locations of the leading liquid front. The numerical results are compared with the experimental data in [22]. From this figure, we observe that the numerical speed is slower than the experimental speed. The reason for the difference is that in the current calculation the density ratio between liquid and gas is about 2.8, whereas the experimental data were obtained for water and air, and their density ratio is about 800. Therefore, the relative aerodynamic resistance is much higher in the current study. Figure 7 displays a very interesting wave structure. The oscillations at the liquid–gas interface are coming from the violent phase transition. Even though the implementation of the surface tension may alleviate this problem, the sharp transition with 2–3 grid points at the interface makes it very difficult to correctly discretize the surface tension term. To correctly capture the density gradient and $\kappa\rho\nabla\nabla^2\rho$ term in the momentum equation, one needs to put a sufficient number of grid points in the “mixed” region. For a real fluid interface, which

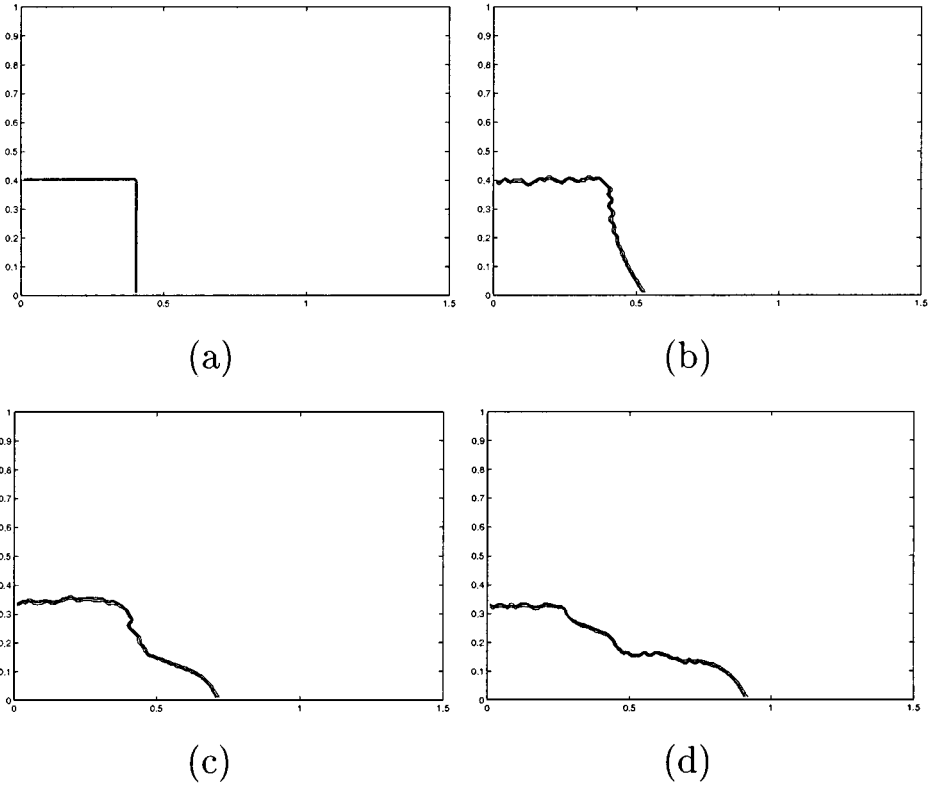


FIG. 7. Liquid-gas interfaces at different output times. (a) $t = 0.0$; (b) $t\sqrt{G/a} = 0.5$; (c) $t\sqrt{G/a} = 1.0$; (d) $t\sqrt{G/a} = 1.5$.

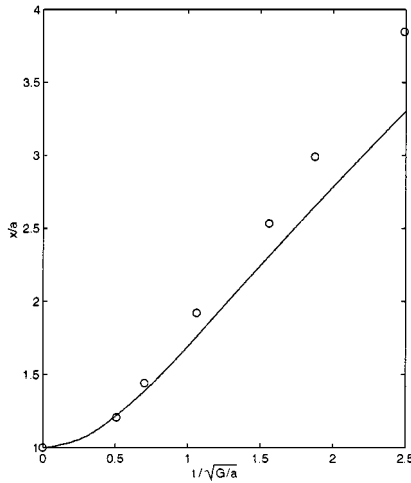


FIG. 8. The horizontal axis is $t\sqrt{G/a}$ and the vertical axis is x/a , where x is the location of the leading liquid front. The solid line is the time evolution of the leading liquid front. The density ratio between liquid and gas is around 2.8. The circle is the experimental data in [22], where real water and air with density ratio around 800 were used.

would have a thickness on the order of nanometers, an extremely refined mesh is needed there. However, the main concern, and also the limitation of the current approach, is to capture the sharp interface, rather than obtain a physical transition inside the layer.

Case 6. This test case is about the collision of two droplets. Similar to the last case, the initial densities of the liquid and gas phases are assigned the theoretical values again from the Maxwell construction, i.e., $1/\rho_l = 0.494273$ and $1/\rho_g = 1.405065$. The cell size used in this case is $\Delta x = \Delta y = 1/100$. The initial droplets with radius $R = 0.055$ are moving toward each other with a velocity magnitude of $U = 0.125$. No gravity is included in this case. The surface tension in this case is included through the term $\kappa\rho\nabla\nabla^2\rho$. Figure 9 shows the time evolution of the droplets. The collision and merging of the droplets can be observed.

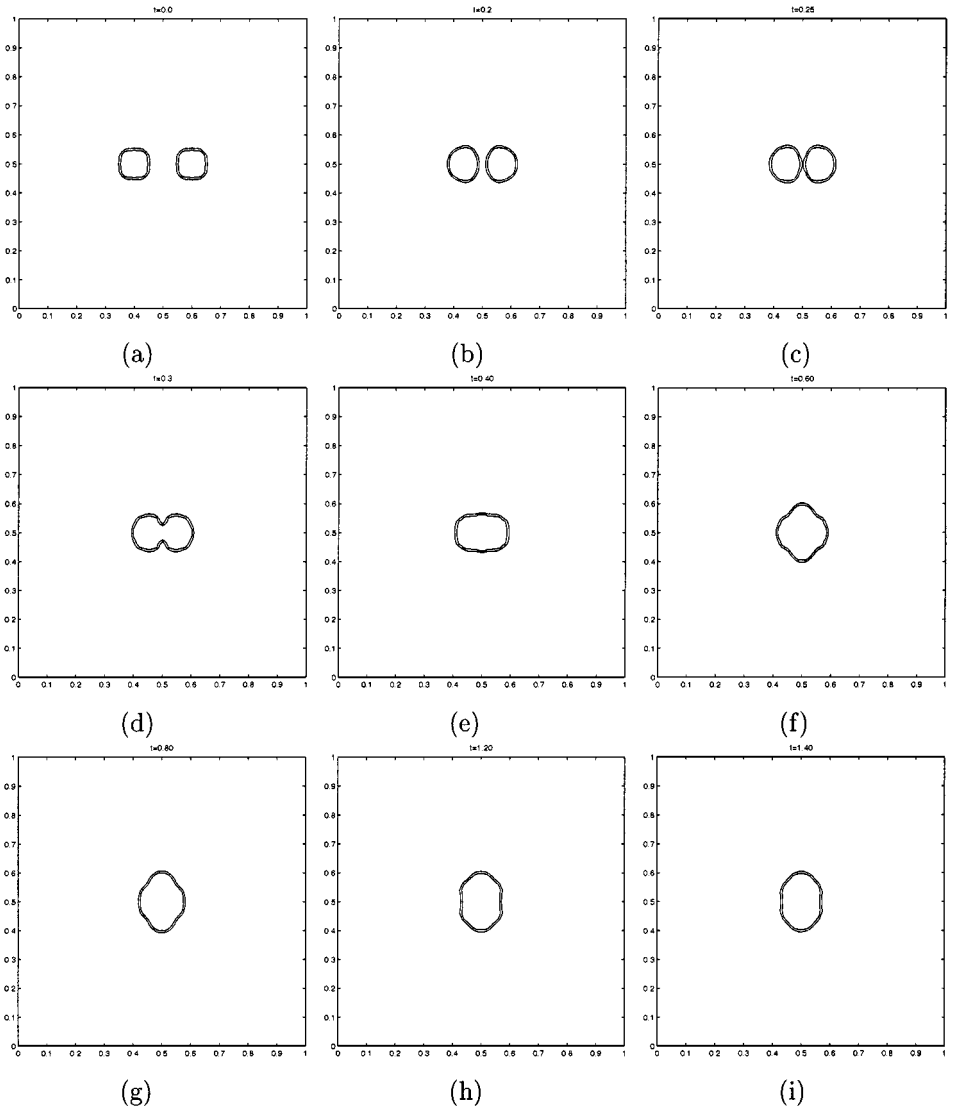


FIG. 9. Time evolution of the collision of two droplets. The output times are (a) $t = 0$, (b) $t = 0.2$, (c) $t = 0.25$, (d) $t = 0.3$, (e) $t = 0.40$, (f) $t = 0.60$, (g) $t = 0.80$, (h) $t = 1.20$, and (i) $t = 1.60$.

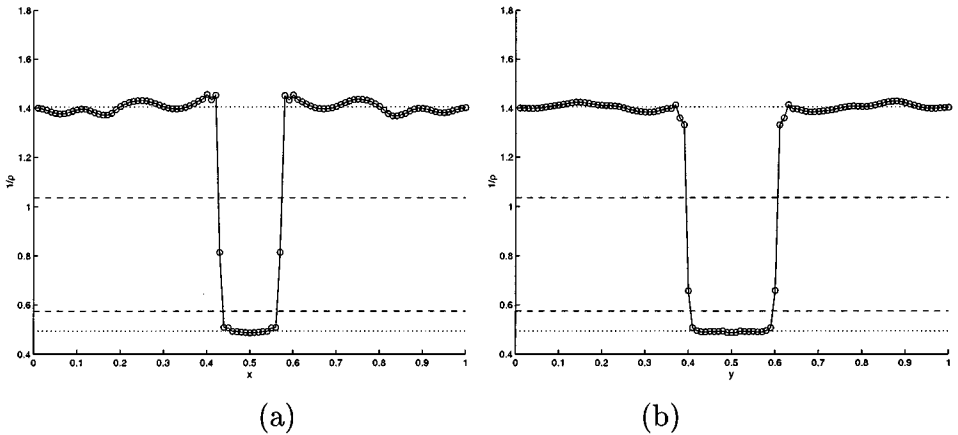


FIG. 10. The distribution $1/\rho$. (a) along the central line of Fig. 9i in the x direction and (b) along the central line of Fig. 9i in the y direction. Since both the liquid and gas are treated as the compressible flow in the current study, small-density fluctuations appear in the dynamical transport process, especially in the gas phase.

Because of the steepening mechanism at the fluid interfaces from the van der Waals EOS, the sharp interface is retained in the time evolution process. Figure 10 shows the density distribution across the central lines in both the x and the y directions of Fig. 9i, where the phase boundaries keep 2 mesh points even though 1,600 time steps have passed at that output time.

5. DISCUSSION AND CONCLUSION

In this paper, we have constructed a kinetic scheme for the hyperbolic–elliptic system, where the van der Waals equation of state is used to describe the phase transition. Owing to the evaporation and condensation process for the fluid in the elliptic region, the liquid–gas interface is captured sharply in the current scheme. Many test cases validate the current approach.

Since the interface in multiphase and multifluid flow is a very complicated dynamical system, any scheme has its limitations. The current paper is only a starting point for studying multiphase flow by solving the mixed type equations. The limitations of the current method include:

1. The current scheme is limited by a condition $p/\rho > 0$. This condition may not be satisfied under certain physical circumstances.
2. The current scheme allows a phase transition to occur, which means that the mass of the individual component cannot be exactly conserved. Also, the effect of latent heat release in the phase transition is not included in the current approach owing to the absence of the energy equation.
3. The viscous effect in the phase transition process is only obtained through numerical dissipation and diffusion in the current scheme. The numerical liquid–gas interface has a much larger scale than the real physical thickness of water and air at atmospheric pressure. Therefore, the surface tension involved through $\kappa\rho\nabla\nabla^2\rho$ is only applicable to the study of surface tension close to the critical region. The study of numerical dissipation on the interface structure needs further investigation.

4. Besides the equilibrium description from the van der Waals EOS, this method is only limited to the flow close to the critical point region. The density ratio used is only on the order of 2–5. Because of the stiffness of the equation, using the van der Waals EOS to simulate high-density ratio two-phase flow is extremely difficult. Physically, the validity of using a macroscopic EOS for describing high-density phase transitions remains an open question. A microscopic description such as one that uses molecular dynamics, is probably necessary.

Even with the many weaknesses and limitations, the preliminary results presented in this paper are very promising and encouraging. In contrast to many other approaches, such as level set and VOF methods, there is no need for tracking, index functions, or any special treatment around the multifluid interfaces. The advantage of using this kinetic approach for the hyperbolic–elliptic equations is due to the fact that a Riemann solution is extremely difficult to obtain for a nonhyperbolic system. The current method is the beginning in the development of more physical approaches for describing multiphase flow. Since the modeling of interfacial phenomena associated with surface tension is one of the most challenging problems for computational methods of multiphase flows, any numerical treatment should have a physical basis; otherwise erroneous solutions can be easily generated in the simulation of such a complicated system.

ACKNOWLEDGMENTS

The author thanks X.Y. He, L.S. Luo, and M. Salas for helpful discussions and suggestions about multiphase flow problems and thanks the referees for their rigorous comments. This research was supported in part by the National Aeronautics and Space Administration under NSAS Contract No. NAS1-97046 while the second author was in residence at the Institute for Computer Applications in Science and Engineering (ICASE), NASA Langley Research Center, Hampton, VA 23681-2199. Additional support was provided by the Hong Kong Research Grant Council through DAG98/99.SC22 and HKUST6132/00p.

REFERENCES

1. D. M. Anderson, G. B. McFadden, and A. A. Wheeler, Diffuse-interface methods in fluid mechanics, *Annu. Rev. Fluid Mech.* **30**, 139 (1998).
2. P. L. Bhatnagar, E. P. Gross, and M. Krook, A model for collision processes in gases I: Small amplitude processes in charged and neutral one-component systems, *Phys. Rev.* **94**, 511 (1954).
3. S. Benzoni-Gavage, Stability of subsonic planar phase boundaries in a van der Waals fluid, *Arch. Ration. Mech. Anal.* **150**, 23 (1999).
4. R. K. Chan, A generalized arbitrary Lagrangian–Eulerian method for incompressible flows with sharp interfaces, *J. Comput. Phys.* **58**, 311 (1975).
5. Y. C. Chang, T. Y. Hou, B. Merriman, and S. Osher, A level set formulation of Eulerian interface capturing methods for incompressible fluid flows, *J. Comput. Phys.* **124**, 449 (1996).
6. S. Chapman and T. G. Cowling, *The Mathematical Theory of Non-Uniform Gases* (Cambridge University Press, Cambridge, UK, 1990).
7. Y. Chen, S. Teng, T. Shukuwa, and H. Ohashi, Lattice-Boltzmann simulation of two-phase fluid flows, *Int. J. Mod. Phys. C* **9**, 1383 (1998).
8. I. L. Chern, J. Glimm, O. McBryan, B. Plohr, and S. Yaniv, Front tracking for gas dynamics, *J. Comput. Phys.* **62**, 83 (1986).
9. B. Cockburn and H. Gau, A model numerical scheme for the propagation of phase transitions in solids, *SIAM J. Sci. Comput.* **17**, 1092 (1996).

10. H. Fan, Traveling waves, Riemann problems and computations of a model of the dynamics of liquid/vapor phase transitions, *J. Diff. Eqn.* **150**, 385 (1998).
11. N. G. Hadjiconstantinou, A. Garcia, and B. J. Alder, The surface properties of a van der Waals fluid, *Physica A* **281**, 337–347 (2000).
12. H. Hattori, *The Riemann Problem of a System for a Phase Transition Problem*, International Series of Numerical Mathematics (1999), Vol. 129, pp. 455–464, Boston, Birkhauser Verlag.
13. X. He, X. Shan, and G. D. Doolen, A discrete Boltzmann equation model for nonideal gases, *Phys. Rev. E* **57**, R13 (1998).
14. X. Y. He, S. Y. Chen, and R. Y. Zhang, A lattice Boltzmann scheme for incompressible multiphase flow and its application in simulation of Rayleigh–Taylor instability, *J. Comput. Phys.* **152**, 642 (1999).
15. C. W. Hirt and B. D. Nichols, Volume of fluid (VOF) method for the dynamics of free boundaries, *J. Comput. Phys.* **39**, 201 (1981).
16. D. Y. Hsieh and X. P. Wang, Phase transition in van der Waals fluid, *SIAM J. Appl. Math.* **57**, 871 (1997).
17. R. Issa and O. Ubbink, Numerical prediction of Taylor bubble dynamics using a new interface capturing technique, in *Proceedings of the 3rd ASME/JSME Joint Fluid Engineering Conference*, FEDSM99-7103 (1999).
18. S. Jin, Numerical integrations of systems of conservation laws of mixed type, *SIAM J. Appl. Math.* **55**, 1536 (1995).
19. F. J. Kelecy and R. H. Pletcher, The development of a free surface capturing approach for multidimensional free surface flows in closed containers, *J. Comput. Phys.* **138**, 939 (1997).
20. J. L. Lebowitz and O. Penrose, Unified theory of lattice Boltzmann model for nonideal gases, *J. Math. Phys.* **7**, 98 (1966).
21. L. Luo, Unified theory of lattice Boltzmann model for nonideal gases, *Phys. Rev. Lett.* **81**, 1618 (1998).
22. J. C. Martin and W. J. Moyce, An experimental study of the collapse of liquid columns on a horizontal plane, *Philos. Trans. R. Soc. London A* **244**, 312 (1952).
23. B. T. Nadiga and S. Zaleski, Investigation of a two-phase fluid model, *Eur. J. Mech. B/Fluids* **15**, 885 (1996).
24. S. Osher and J. A. Sethian, Fronts propagating with curvature dependent speed: Algorithms based on Hamilton–Jacobi formula, *J. Comput. Phys.* **79**, 12 (1988).
25. D. H. Rothman and S. Zaleski, Lattice-gas models of phase separation: Interface, phase transitions and multiphase flow, *Rev. Mod. Phys.* **66**, 1417 (1994).
26. X. Shan and H. Chen, Simulation of non-ideal gases and liquid-gas phase transitions by the lattice Boltzmann equation, *Phys. Rev. E* **49**, 2941 (1994).
27. C. W. Shu, A numerical method for systems of conservation laws of mixed type admitting hyperbolic flux splitting, *J. Comput. Phys.* **100**, 424 (1992).
28. M. Slemrod, Admissibility criteria for propagating phase boundaries in a van der Waals fluid, *Arch. Ration. Mech. Anal.* **81**, 301 (1983).
29. M. Slemrod and J. E. Flaherty, Numerical investigation of a Riemann problem for a van der Waals fluids, in *Phase Transformation*, edited by C. A. Elias and G. John, 203–212 (Elsevier, New York, 1986).
30. H. B. Stewart and B. Wendroff, Two-phase flow: Models and methods, *J. Comput. Phys.* **56**, 363 (1984).
31. M. Sussman, P. Smereka, and S. Osher, A level set approach for computing solutions to incompressible two-phase flow, *J. Comput. Phys.* **114**, 146 (1994).
32. M. R. Swift, W. R. Osborn, and J. M. Yeomans, Lattice Boltzmann simulation of nonideal fluids, *Phys. Rev. Lett.* **75**, 830 (1995).
33. B. van Leer, Towards the ultimate conservative difference scheme IV, a new approach to numerical convection, *J. Comput. Phys.* **23**, 276 (1977).
34. K. Xu, *Gas-Kinetic Schemes for Compressible Flow Simulations*, 29th CFD Lecture Series 1998–03 (Von Karman Institute, Belgium, 1998).
35. R. W. Yeung, Numerical methods in free surface flows, *Annu. Rev. Fluid Mech.* **14**, 395 (1982).